Biomass Conversion and Biorefinery (2026) 16:40
https://doi.org/10.1007/s13399-025-06977-9

ORIGINAL ARTICLE

Pore-engineered okra stem derived activated carbon with large surface area for high-performance supercapacitors

Wen Li[1] · **Mingyu Wu**[2] · **Zejian Chen**[1] · **Jianxiong Zhao**[1] · **Rongke Sun**[1] · **Xiao Zhang**[1] · **Dongliang Ma**[2] · **Yanqing Ma**[1,3,4,5] · **Lei Ma**[1,3,5]

Received: 20 March 2025 / Revised: 29 October 2025 / Accepted: 18 November 2025

Abstract

Biomass-derived microporous carbon-based supercapacitors have recently gained considerable attention, primarily due to their exceptional cost-efficiency and significant contribution to promoting social sustainability. In this study, the long-fiber plant okra stem was selected as a precursor for carbon materials. Utilizing its natural channels, microporous carbon electrode materials were successfully synthesized through direct pyrolysis combined with KOH activation. The optimized carbon electrode was then used to fabricate a symmetric supercapacitor. At a relatively low activation temperature of 500 °C, the symmetric supercapacitor exhibited excellent electrochemical performance. The specific capacitance reached 100.3 F g^{-1} when tested at a current density of 0.2 A g^{-1}. Furthermore, after 10,000 charge-discharge cycles at a current density of 2 A g^{-1}, the supercapacitor retained 97% of its original capacitance, demonstrating outstanding cycling stability. This configuration not only enhanced the overall performance and durability but also significantly improved safety, making it well-suited for applications in electronic devices.

Keywords Okra stem · Supercapacitor · Microporous carbon · Structure-activity relationship

1 Introduction

In recent times, the escalating global energy and environmental challenges have highlighted the urgent need for developing energy storage systems that integrate sustainability with high-efficiency energy conversion [1]. Compared to traditional battery storage systems, supercapacitors are increasingly recognized as an ideal solution for future energy storage technology, thanks to their rapid charge/discharge capabilities, large capacity, extended lifespan, and superior environmental sustainability [2]. In the design of supercapacitors, carbon-based electrodes are essential components that significantly impact the device's overall performance. The characteristics of these electrodes are key to determining the energy storage capacity and efficiency of supercapacitors, making them a focal point for technological development and optimization. Carbon-derived materials are distinguished by their superior electrical conductivity, expansive specific surface area, and intricate hierarchical pore architecture. These characteristics allow them to consistently deliver exceptional capacitive performance while maintaining robust long-term stability, making them highly suitable for advanced energy storage applications. Additionally, the robust framework of carbon materials provides enhanced mechanical durability, allowing them to maintain structural integrity and functionality through numerous charge-discharge cycles [3].

In order to further improve the performance of supercapacitors and broaden their application scope, researchers

---

Wen Li and Mingyu Wu contributed equally to this work.

✉ Yanqing Ma
mayanqing@tju.edu.cn

✉ Lei Ma
lei.ma@tju.edu.cn

[1] Tianjin International Center for Nanoparticles and Nanosystems, Tianjin University, Tianjin 300072, PR China

[2] School of Materials Science and Engineering, Xinjiang University, Urumqi 830017, PR China

[3] Tianjin Key Laboratory of Low-dimensional Electronic Materials and Advanced Instrumentation, Tianjin 300072, PR China

[4] School of Precision Instrument and Opto-electronics Engineering, Tianjin University, Tianjin 300072, PR China

[5] Haihe Laboratory for Low-dimensional Electronic Materials, Add 1 to No.57, Wujiayao Street, Hexi District, Tianjin 300074, PR China

are increasingly focusing on the precursor materials of carbon electrodes in supercapacitors, especially those low-cost and environmentally friendly materials [4]. Compared with advanced materials such as traditional carbon nanotubes, graphene, and conductive polymers, biomass derived carbon materials have received great attention due to their cost-effectiveness, wide availability, and environmental friendliness [5]. These materials provide a feasible and sustainable alternative as precursors for carbon electrodes in supercapacitors [6, 7]. For supercapacitors, the three most important factors affecting capacitive performance are specific surface area (S_{BET}), electrode resistance (R_S) and pore volume (V_{tot}), as has been well-established in previous machine learning studies [2, 7, 8]. Biomass-derived carbon materials are particularly well-suited for electrodes with excellent electrochemical performance, as they inherently possess these desirable characteristics. Moreover, the unique vascular structure of these plants plays a critical role in facilitating the efficient transport and adsorption of electrolyte ions, which is essential for enhancing the performance of supercapacitors. By leveraging the naturally arranged channels within these structures, the pore network can be further optimized, reducing energy and material losses during electrochemical reactions and maximizing the adsorption of electrolyte ions [9–12].

Okra is a herbaceous plant belonging to the Malvaceae family, characterized by a vascular bundle structure where the top and bottom of the bundle are interconnected, facilitating the penetration of activators [6]. The inner walls of these bundles feature numerous sieve pores that facilitate the transport of electrolyte ions, making them ideal for the creation of porous carbon materials in energy storage systems [2]. Various lignocellulosic residues, such as cotton stover [13], corn stover [14], and soybean stover [15], have been investigated as sustainable carbon precursors for supercapacitors. Compared to these feedstocks, okra stems have a high cellulose content (α-cellulose content (67.5%), moderate hemicellulose content (15.4%), and relatively low lignin content (7.1%)), and its high content of cellulose and hemicellulose is more conducive to the formation of activated carbon with microporous/mesoporous structure [16, 17]. Furthermore, most of the available studies on okra have focused on the pods or seeds [18], while the stem remains an abundant but underutilized agricultural by-product [19]. Therefore, selecting okra stems as a precursor for carbon material preparation presents a twofold advantage of waste minimization and enhanced cost efficiency. This study involved the utilization of okra stem waste as a carbon source, transforming it into carbon electrodes for supercapacitors. The influence of activation temperature on the surface morphology and structural characteristics of the resultant biochar was comprehensively examined. Extensive electrochemical analyses were conducted to evaluate the electrochemical performance of the biochar. The findings indicate that the carbon material derived from okra stems serves as a cost-effective electrode with significant potential for high-efficiency energy storage in supercapacitors. Moreover, the conventional temperature range for KOH activation of biochar typically falls between 700 °C and 900 °C [20–26]. However, this study identified an optimal activation temperature of 500 °C for okra-derived carbon, significantly lower than the conventional activation temperatures for other carbon materials. This reduced activation temperature not only conserves energy but also provides significant cost advantages, effectively lowering production expenses. Overall, the findings suggest that carbon materials derived from okra stems exhibit excellent electrochemical performance at low cost, making them a promising material for high-performance supercapacitor applications.

2 Experimental section

2.1 Materials

Okra stems were collected from vegetable field in Tianjin, China. Potassium hydroxide (KOH) was sourced from Tianjin Damao Chemical Reagent Factory, while acetylene black and polytetrafluoroethylene (PTFE) were supplied by Tianjin Aiweixin Chemical Technology Co. Ltd. All reagents used in the experiment were applied directly without any further purification.

2.2 Synthesis of okra stem-based carbon

The okra stem was freeze-dried under vacuum. After freeze-drying, the okra stems were pre-charred in a tube furnace. The okra stems were heated from room temperature to 400 °C in Ar atmosphere at a rate of 5 °C min^{-1} and held for 1 hour and be named as AC. Pre-carbonization temperature was determined by thermogravimetric (TG) test (Fig. S1). The KOH activation method catalyzes the rearrangement of carbon atoms and the formation of highly microporous structures, functional groups, and graphitized structures on the surface of carbon materials through the intercalation of potassium ions between the lattices, the synergistic oxidation of the carbon elements, and the in-situ generation of CO_2 in the high-temperature process for the activation of carbon [27–29]. Therefore, KOH was chosen as the activator in this study. AC was mixed with KOH at a mass ratio of 1:4, and an appropriate amount of deionized water was added to form a mixed solution, which was dried in an oven at 60 °C for 12 hours. The dried mixture was put into a tubular furnace, heated to various target temperatures at a rate of 5 °C min^{-1}

in Ar atmosphere, and held for 1 hour. Subsequent to cooling back to room temperature at the same rate, the products were thoroughly washed with 0.1 M HCl solution and deionized water until reaching neutral pH. Following drying in an oven at 80 °C for 12 hours, these materials were designated as PC-*x*, with ‘*x*’ representing the different activation temperatures (400, 500, 600, 700, 800, and 900 °C). The entire preparation process of PC-*x* is illustrated in Scheme 1.

2.3 Structural measurements

Testing methods included a scanning electron microscope (SEM, SU3500, Hitachi), a X-ray diffraction (XRD, Bruker, Cu-Kα, λ = 1.54060 Å), a Raman spectrometer (RTS-2, Titan Electro-Optics (Hong Kong) Limited, 532nm), The decomposition temperature of the PC-500 material was assessed through thermogravimetric analysis (TGA) using a Mettler Toledo TG2 instrument, Determine the specific surface area and pore size distribution of PC-500 using the Brunauer Emmett Teller (BET) method combined with N_2 adsorption desorption isotherm.

2.4 Electrochemical test

Mix the synthesized porous carbon-based material thoroughly with PTFE and acetylene black in a mass ratio of 8:1:1. The slurry is compressed into thin sheets using a roller press, after which the carbon film, measuring 0.8 × 0.8 cm², is pressed onto foam nickel under a pressure of 10 MPa to form the carbon electrode. In the three-electrode setup, the carbon electrode functions as the working electrode, the Hg/HgO electrode as the reference, and Pt foil as the counter electrode. A 6 M KOH solution is used as the electrolyte during electrochemical testing. At room temperature, several electrochemical tests were performed using the CHI760E electrochemical workstation, including cyclic voltammetry (CV) at scan rates ranging from 2 to 100 mV/s, constant current charge-discharge (GCD) at current densities between 0.2 and 5 A g^{-1}, and cycle life stability testing. The specific capacitance of the electrode was calculated from the GCD curve using the following Eq.

$$C = \frac{I \times \triangle t}{\triangle V \times m} \tag{1}$$

where C is the specific capacitance (F g^{-1}), I (A) represents the discharge current, Δt (s) is the discharge time; m (g) the mass of the active material, and ΔV (V) the potential window.

In the two-electrode setup, a symmetric supercapacitor was constructed using two identical working electrodes, with 1 M H_2SO_4 serving as the electrolyte. The total supercapacitor can be well defined through the following equation:

$$C_{cell} = \frac{I \times \triangle t}{\triangle V \times m} \tag{2}$$

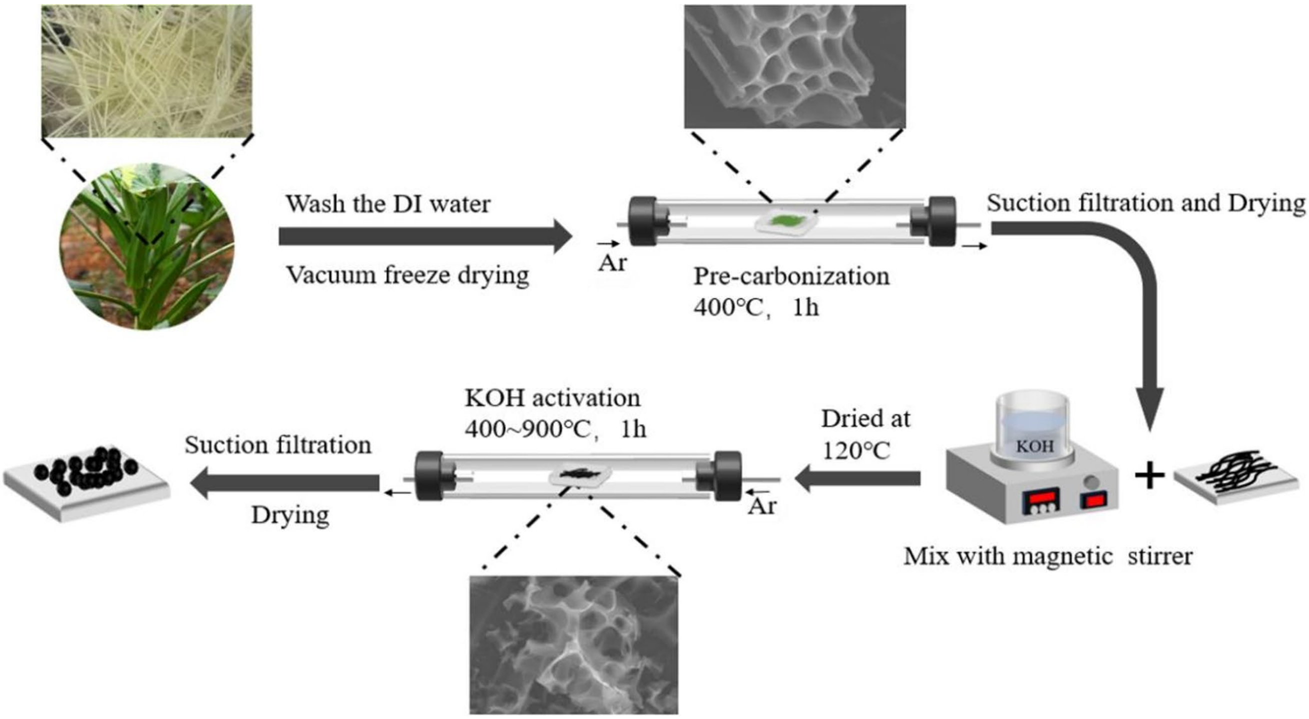

Scheme 1 Schematic of the preparation process of PC-*x*

where C_{cell} (F g^{-1}) is the device specific capacitance, The energy density (E, Wh kg^{-1}) and power density (P, W kg^{-1}) can be calculated by C_{cell} from the following equation:

$$E = \frac{1}{2} C_{cell} \times \triangle V^2 \times \frac{1}{3.6} \tag{3}$$

$$P = \frac{E}{\triangle t} \times 3600 \tag{4}$$

Electrochemical impedance spectroscopy (EIS) measurements were carried out at open circuit potential with a 10 mHz to 100 kHz sinusoidal signals at an amplitude of 5 mV.

3 Results and discussions

Figure 1 illustrates the morphology of okra stem phloem fibers in their raw, pre-carbonized, and activated states. In the raw phloem fibers of the okra stem (Fig. 1a-b), a well-defined long-range ordered structure is observed in the sieve tube, along with the sieve holes in the tube wall, indicating the presence of numerous vascular bundles and hollow tubes. These interconnected hollow structures form a porous scaffold crucial for subsequent carbonization and activation processes, and it retains the original carbon skeleton well after carbonization(Fig. 1c). It exhibits directional channels with interconnected layered pores. The emergence of these directional channels aids in speeding up ion transport, while the interconnected pore network notably shortens the ion transport pathway, significantly enhancing ion diffusion/transport efficiency [30]. These features play a vital role in facilitating electrolyte penetration and creating more electrochemically active sites, thereby enhancing the material's electrochemical performance. The SEM image depicted in Fig. 1d corresponds to an activation temperature of 400 °C. The image reveals a relatively smooth and compact surface structure with some small, evenly distributed pores of modest size. However, the pore volume and specific surface area remain limited, suggesting incomplete activation at 400 °C, resulting in reduced porosity. At an activation temperature of 500 °C, the sample surface undergoes significant structural transformations, exhibiting a notable increase in pore quantity with a moderately distributed pore size (Fig. 1e). The surface displays regular macropores and mesopores, forming an interconnected porous network that enhances the specific surface area and electrolyte permeability. This feature promotes rapid ion diffusion and efficient energy storage. In addition, the atomic composition of the PC-500 sample is as follows: 73.71% C and 26.29% O, indicating that biomass is decomposed by the activator during the pyrolysis activation process. The results in the formation of a porous structure enriched with defects and oxygen-containing functional groups. It increases the wettability between the electrode/electrolyte and reduces the interfacial resistance. Furthermore, it can enhance the electrolyte accessibility and ionic adsorption/desorption, and thus improves the overall electrochemical performance [31, 32].Upon reaching 600 °C, the sample's surface pores further expand, but pore size distribution becomes uneven, leading to areas of excessive activation with oversized pores and voids (Fig. 1f). As the temperature rises to 700 ℃, the

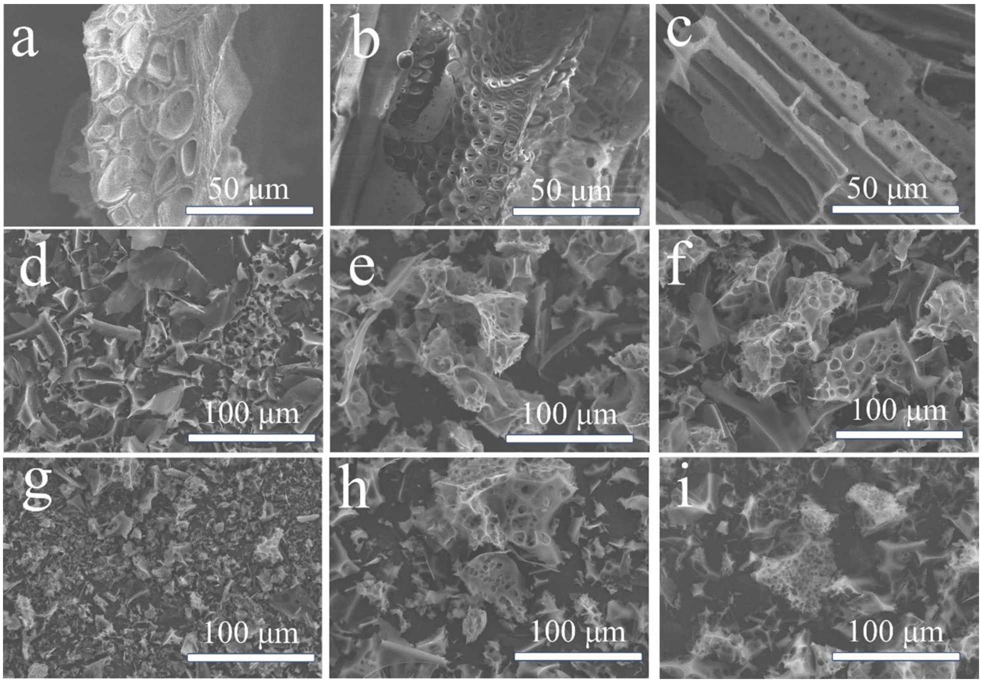

Fig. 1 SEM Characterization of samples: raw phloem fibers of the okra stem (**a**, **b**); pre-carbonized okra stem (**c**); PC-400 (**d**); PC-500 (**e**); PC-600 (**f**); PC-700 (**g**); PC-800 (**h**); PC-900 (**i**)

degree of porosity significantly increases, and more large pores and disordered structures begin to form. The pores in some areas have become excessively coarse, resulting in a rough surface morphology of the material. The distribution of pores is no longer uniform, and chaotic carbon sheet stacking layers have appeared (Fig. 1g). This phenomenon is mainly due to excessive activation caused by high temperature, leading to the destruction and instability of carbon structure. As the temperature further increases, at 800 °C, the pore structure of the sample becomes more irregular, showing severe signs of over activation. Most of the pores became extremely loose, and some areas showed damage or "hollow" structures (Fig. 1h). This excessively high activation temperature weakens the overall structure and mechanical strength of the material. At a high temperature of 900 °C, the pore structure of the sample reached its most loose state, and the pore morphology in some areas almost completely disappeared, presenting a large number of large pores and cracks on the surface (Fig. 1i) [33]. At this point, the overall structure of the sample becomes extremely fragile, ultimately forming thin and porous carbon sheets.

XRD and Raman analyses were conducted to examine the structural characteristics of six samples prepared at different activation temperatures. In Fig. 2a, the primary crystal structure of the activated carbon sample is depicted through XRD. The carbon materials prepared at 400, 500, and 600 °C exhibit a broad peak around 25° corresponding to the (002) plane diffraction of disordered carbon, indicating its non-crystalline nature [34]. As the activation temperature rises from 700 °C to 900 °C, the intensity of the characteristic XRD peak of the biochar sample notably diminishes, and the peak width increases, suggesting that higher activation temperatures result in crystal structure disruption and the introduction of more defects [35]. To further assess the impact of activation temperature on the graphitization level of the produced carbon, Raman spectroscopy was employed to analyze the synthesized activated carbon, as shown in Fig. 2b. Notably, two distinct peaks were identified at 1356 cm^{-1} (D band) and 1579 cm^{-1} (G band). The strong D band typically indicates the presence of structural imperfections in amorphous carbon, while the G band signifies the sp^2 hybridized graphite carbon structure, denoting ordered graphite layers or planar carbon atom arrangements within the materials [36]. The ratio of the intensities of the D and G bands (I_D/I_G) is recognized to reflect the disorder or graphitization level of carbon materials: a higher ratio implies more defects, indicating a lower degree of structural order [37].

The I_D/I_G ratios of PC-*x* (x = 400, 500, 600, 700, 800, and 900 °C) were 0.905, 0.857, 0.954, 0.978, 0.983, and 1.045, respectively. A marked reduction from 0.905 at 400 °C to 0.857 at 500 °C reflects the suppression of structural disorder and the development of more ordered graphitic domains. This trend is associated with a relative weakening of the D band, suggesting that controlled activation at 500 °C facilitates the rearrangement of amorphous carbon into locally ordered sp^2 networks. Beyond this temperature, however, the I_D/I_G ratio increases progressively, reaching 1.045 at 900 °C, which indicates the reemergence of disorder. Such behavior can be attributed to overactivation at elevated temperatures, where excessive etching and carbon chain scission disrupt the lattice and generate new defect sites [38]. These results highlight the dual role of thermal treatment: moderate activation promotes graphitization and enhances electrical conductivity, whereas excessive activation undermines structural integrity by introducing defects. Consequently, the 500 °C sample achieves the most favorable balance, combining a high degree of graphitization with structural stability, which directly underpins its superior capacitive performance.

To further characterize the chemical composition and surface functional groups of the porous carbon material, the PC-500 sample was analyzed using XPS. The high-resolution C1s spectrum (Fig. S2a) can be divided into three peaks located at ~ 284.5, 286.2, and 288.1 eV, corresponding to sp^3-C, C-O, and C = O, respectively, and the contents of C-O and O-C = O are 28.78% and 18.72%, respectively

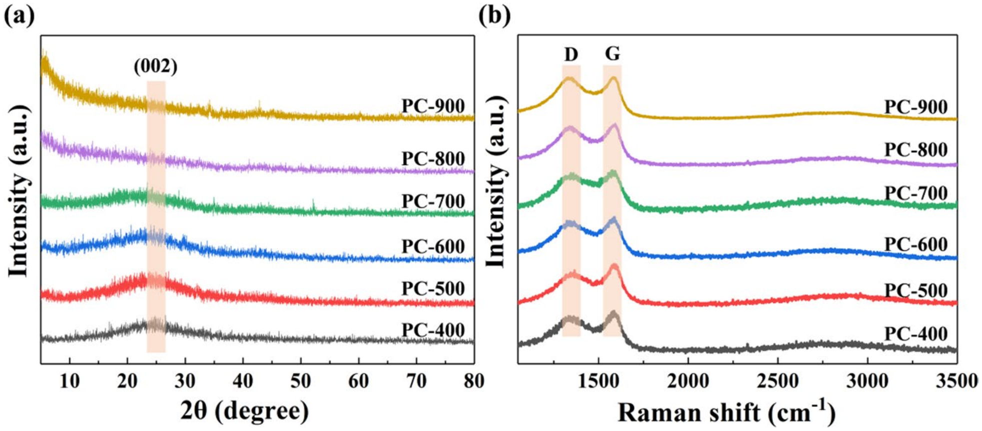

Fig. 2 (**a**) XRD patterns and (**b**) Raman spectra of PC-x (x = 400, 500, 600, 700, 800 and 900 °C)

[39, 40]. This high oxygen content increases the wettability between the electrolyte and the electrode and enhances the conductivity, which improves the electrochemical performance [41]. O 1 s XPS spectra (Fig. S2b) can be divided into two peaks with binding energies of 533.8 and 535.6 eV, which correspond to ether oxygen (C-O-C) and carboxylic acid functional groups (COOH), respectively [39].

The pore characteristics of PC-500 were evaluated via N_2 adsorption-desorption analysis at 77 K. The N_2 adsorption isotherm for the PC-500 samples, as shown in Fig. 3a, distinctly aligns with the classic Type I isotherm characteristics. Within the low-pressure range (< 0.1), there is a rapid increase in adsorption, indicating a significant presence of micropores in the PC-500 sample, enhancing the provision of active sites for electrochemical applications [42]. A summary of the textural properties of PC-500 is presented in Table 1, revealing an exceptionally high surface area of 1216 $m^2\ g^{-1}$. Figure 3b depicts the pore size distribution of the PC-500 sample, highlighting a prevalent pore size of approximately 1 nm, indicative of a predominantly microporous structure. The pore size distribution curve indicates that the highest volume of pores falls within the range of 0.6 nm to 2 nm. This microporous-dominated pore structure facilitates the smooth entry and exit of electrolyte ions and shortens the electron transfer path. It can effectively promote the charge transfer process of reversible ion adsorption/desorption and thus enhance the specific capacitance. Furthermore, the short diffusion paths provided by micropores allow for a higher utilization of the accessible surface area under low-to-moderate current densities, in agreement with previous reports that optimized micropore size is critical for maximizing charge storage capability in carbon-based supercapacitor [43].

Table 1 The parameters of pore structure of PC-500.

Sample	S_{BET}($m^2\ g^{-1}$)	V_{total}($cm^3\ g^{-1}$)	V_{micro}($cm^3\ g^{-1}$)	V_{micro}/V_{total}(%)
PC-500	1216	0.42	0.41	97.6

To evaluate the electrochemical behavior of the samples prepared at different carbonization temperatures, cyclic voltammetry (CV) and galvanostatic charge–discharge (GCD) measurements were conducted in a three-electrode configuration using 6 M KOH as the electrolyte. As shown in Fig. S3, the CV curves of all samples exhibit approximately rectangular shapes at moderate scan rates, indicating typical double-layer capacitive behavior. Moreover, the GCD curves display symmetric triangular shapes at current densities ranging from 0.2 to 10 A g^{-1} (Fig. S4). These results confirm that the charge storage process primarily arises from electrostatic adsorption of ions at the electrode–electrolyte interface, consistent with an electric double-layer capacitance (EDLC) mechanism [44].

To optimize the application of the synthesized carbon materials in devices, the capacitance performance of PC-*x* was assessed by fabricating symmetric supercapacitors within a two-electrode system. Figure 4 illustrates the cyclic voltammetry (CV) curve of PC-*x* at varying scanning rates from 2 mV s^{-1} to 100 mV s^{-1}, depicting the relationship between voltage fluctuation and response current, thereby elucidating the supercapacitor's electrochemical behavior. As the scanning rate increases in the CV curve of PC-400 (Fig. 4a), the degree of curve distortion intensifies. This effect can be attributed to the lower activation temperature, reduced porosity, and simplified pore structure, leading to heightened charge transfer resistance (as indicated in Table 2). The hindered diffusion of electrolyte ions within the electrode material restricts the charge storage capacity, preventing the formation of a highly symmetrical rectangular curve. Particularly at higher scanning rates, significant curve bending occurs, impeding local charge discharge reactions and resulting in deformation of the CV curve [45]. At an activation temperature of 500 °C, as depicted in Fig. 4b, the CV curve of PC-500 exhibits enhancements compared to PC-400, with a curve shape closer to an ideal rectangle, particularly at lower scan rates. This indicates an improvement in the electrochemical performance of

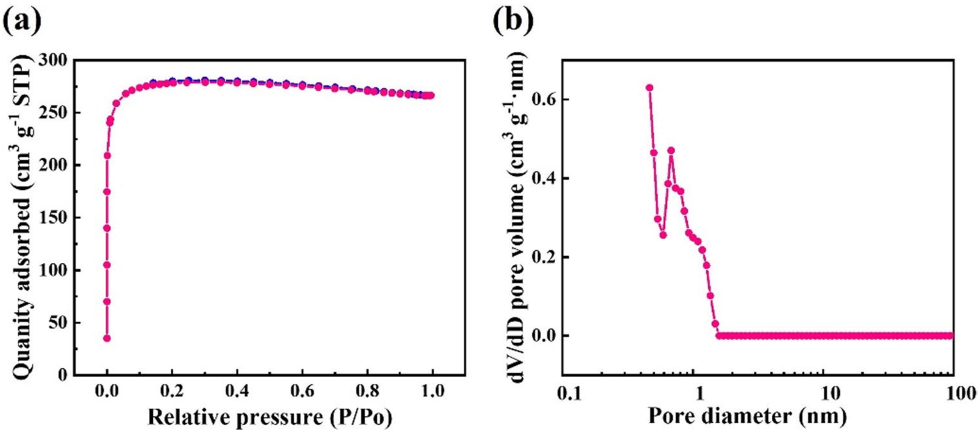

Fig. 3 (**a**) N_2 adsorption-desorption isotherms (77 K) and (**b**) Pore size distribution for PC-500

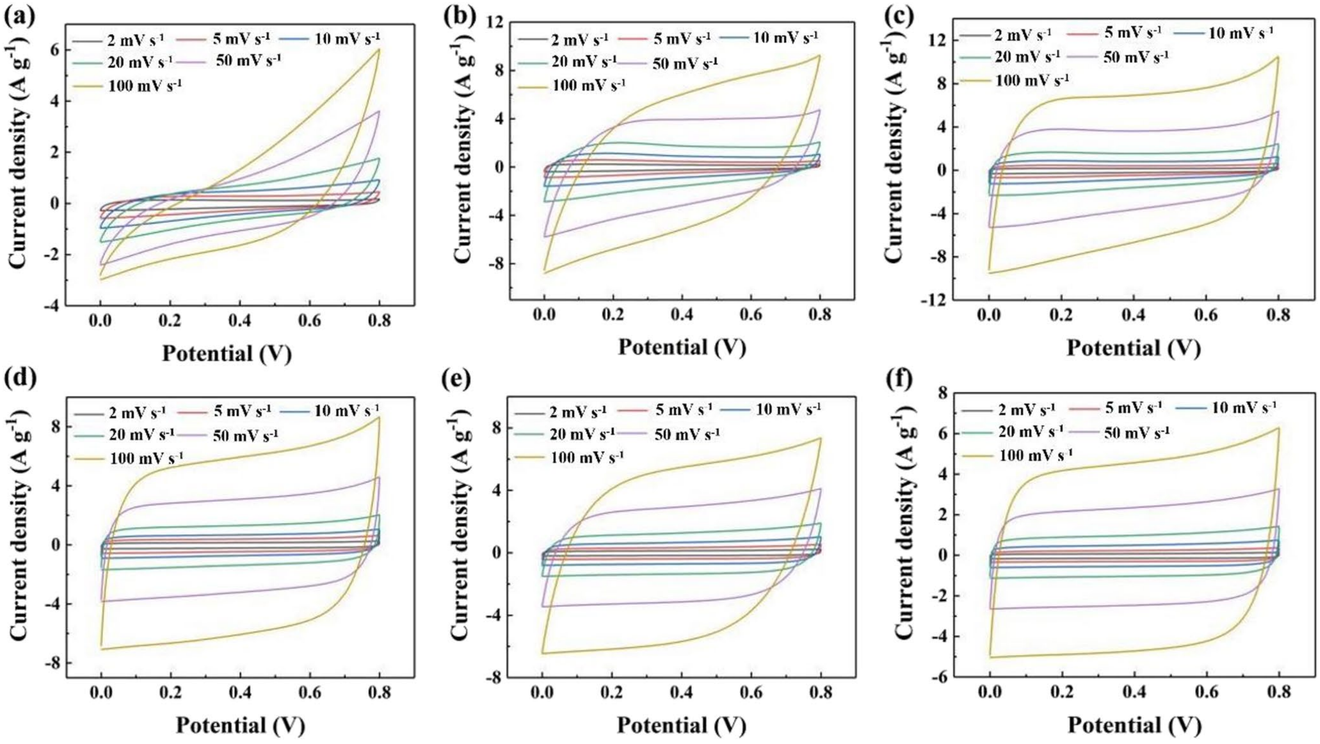

Fig. 4 CV curves of the PC-*x* (*x*=400, 500, 600, 700, 800, and 900 °C) symmetric supercapacitor at various scan rates within the voltage range of 0–0.8 V. **(a)** PC-400, **(b)** PC-500, **(c)** PC-600, **(d)** PC-700, **(e)** PC-800, **(f)** PC-900

Table 2 R_s and R_{ct} parameters for all samples

T(°C)	400	500	600	700	800	900
$R_s(\Omega)$	1.430	1.106	1.413	1.003	2.815	2.558
$R_{ct}(\Omega)$	3.586	2.045	0.020	0.01	0.011	0.051

the material. Even at high scanning rates, while the curve retains some curvature, it appears smoother than that of PC-400, suggesting good charge discharge reversibility. The superior performance can be attributed to the activation temperature of 500 °C, which enhances the porosity of the sample, leading to a more uniform distribution of pores. This facilitates easier penetration of electrolyte ions into the electrode material's pores, thereby enhancing capacitance performance. At this temperature, the material structure exhibits a high degree of order, supporting a rapid ion diffusion rate [46]. As the temperature escalates to 600 °C (Fig. 4c), the CV curve continues its trend towards an ideal rectangle, especially noticeable at low scan rates, approaching typical double-layer capacitor behavior. With further increments in the scanning rate, the curve slightly bends, indicating a degree of charge transfer limitation. In the CV curve of PC-700 (Fig. 4d), as the scanning rate increases, the curve progressively exhibits a higher current response while maintaining good symmetry, implying a more reversible charge storage and release process within the electrode material. However, even at high scanning rates, the curve retains some curvature, pointing to electrochemical kinetic limitations in the charge transfer process. Comparatively, when the temperature rises to 800 °C (Fig. 4e), the curve at lower scanning rates approaches a rectangular shape, showcasing high capacitance characteristics. Nevertheless, at higher scanning rates, the curve displays increased curvature, indicating restricted ion diffusion. Upon reaching 900 °C (Fig. 4f), although the curve maintains good symmetry at lower scanning rates, the curvature significantly intensifies with increasing scan rate, accompanied by a relatively modest current response. This suggests that under the high-temperature activation of 900 °C, excessive activation of the pore structure leads to heightened ion diffusion limitations and decreased electrochemical performance. At a scanning rate of 2 mV s^{-1}, the specific capacitances of the six samples were measured as 66.4, 103.1, 95.9, 90.8, 75.4, and 56.4 F g^{-1}, respectively. Notably, the sample activated at 500 °C exhibited the highest specific capacitance. This underscores that an activation temperature of 500 °C facilitates the formation of rich microporous structures, boosts specific surface area and graphitization degree, thereby offering more electrochemically active sites for the adsorption of electrolyte ions, ultimately yielding a higher specific capacitance [47].

The charge-discharge behavior of the PC-*x* material was evaluated through electrochemical galvanostatic charge-discharge (GCD) measurements, with the outcomes illustrated in Fig. 5. At 400 °C, the GCD curve (Fig. 5a) is asymmetric, with longer discharge time, reflecting sluggish charge transfer due to the low porosity of PC-400 [48]. Moving to 500 °C, the charge-discharge process exhibits a more symmetrical triangular shape, with a flatter curve signifying a more stable charge storage and release process of the electrode material (Fig. 5b). The improved charge transfer performance of the sample indicates enhanced reversibility. Upon reaching 600 °C, the charge-discharge curve maintains good symmetry, demonstrating ideal electrochemical performance (Fig. 5c). At lower current densities, the curve remains stable and approaches an ideal triangular shape. However, with increasing current densities, the curve slightly steepens, indicating a certain impact on the charge transfer speed under high current densities. The elevated porosity resulting from the 600 °C activation temperature facilitates faster penetration of electrolyte ions into the electrode surface, optimizing material conductivity and showcasing favorable charge-discharge characteristics. Examining the GCD curve of PC-700, as the current density rises, the curve steepens, and the charge-discharge process becomes more asymmetric, signaling a gradual limitation in charge transfer speed (Fig. 5d). At higher current densities, the discharge duration noticeably shortens, suggesting limitations in ion diffusion and charge storage capabilities of the electrode material under such conditions. The 700 °C activation temperature increases the sample's porosity, but also leads to the presence of uneven and larger pores, potentially complicating the diffusion and transport paths of electrolyte ions within the electrode, thereby affecting electrochemical performance at high current densities. At 800 °C, with increasing current density, the curve intensifies, and the discharge duration significantly shortens due to the excessively loose pore structure resulting from the activation temperature, leading to irregular structures and large pores in certain areas (Fig. 5e). This may impede electrolyte permeability, elongate ion diffusion paths, and subsequently impact electrochemical performance at high current densities. Upon reaching 900 °C, as the current density escalates, the charge-discharge duration decreases, significantly diminishing the electrochemical performance (Fig. 5f). The pore structure of the sample becomes excessively loose due to the high-temperature activation, resulting in severe over-activation and the presence of uneven, large pores, further hindering electrolyte permeability and ion diffusion rates. At high current densities, the electrochemical performance declines significantly, making effective charge storage nearly unattainable, leading to extremely short discharge

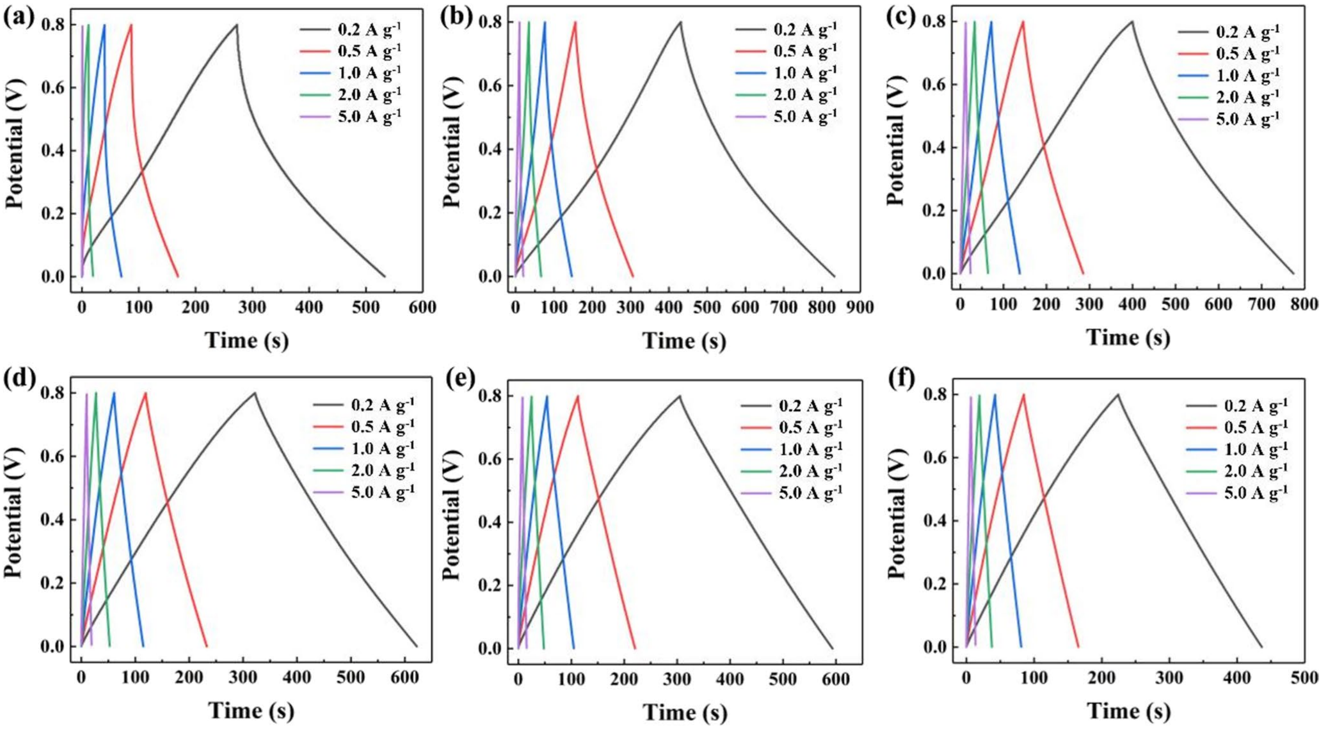

Fig. 5 GCD curves of the PC-x (x = 400, 500, 600, 700, 800, and 900 °C) symmetric supercapacitors at varying current densities within the voltage range of 0–0.8 V. (**a**) PC-400, (**b**) PC-500, (**c**) PC-600, (**d**) PC-700, (**e**) PC-800, (**f**) PC-900

times. The capacitance of PC-*x* (x = 400, 500, 600, 700, 800, and 900 °C) at 0.2 A g^{-1} measures 65, 100.3, 93.4, 75, 72, and 53.1 F g^{-1}, respectively. PC-500 attains the highest capacitance because activation at this temperature produces an optimal balance—abundant microporosity (high accessible surface area) together with preserved channel connectivity and an enhanced degree of graphitization, thus enabling both efficient ion adsorption and favorable electronic conductivity while avoiding the transport penalties associated with excessively large or collapsed pores [49].

Figure 6a shows the variation of specific capacitance of carbon materials with activation temperature at different scanning rates. At low scan rates, such as 2 mV s^{-1}, all samples at different activation temperatures display high specific capacitance, suggesting effective electrolyte ion penetration into the electrode material pores and complete charging and discharging processes, resulting in higher specific capacitance [50]. As the scanning rate increases, the impact of activation temperature on capacitance becomes evident. Samples activated at 500 °C and 600 °C maintain good specific capacitance, whereas the sample activated at 400 °C experiences a significant decrease, likely due to an imperfect pore structure and high charge transfer resistance resulting from low-temperature activation. At higher scanning rates, the specific capacitance of all samples generally decreases due to the limitation on the diffusion rate of electrolyte ions, leading to incomplete charge storage processes. The capacitance retention rates for the six samples are 23%, 42%, 65%, 60%, 59%, and 75%, respectively. These results clearly demonstrate that samples activated at higher temperatures exhibit superior capacitance retention capabilities. The enhanced capacitance retention capabilities observed in samples activated at higher temperatures may be attributed to the formation of well-developed mesoporous and macroporous structures, facilitating rapid ion diffusion and charge storage at elevated scan rates [20].

In Fig. 6b, the specific capacitance of carbon materials is depicted against activation temperature at varying current densities. At low current densities, such as 0.2 A g^{-1}, carbon materials typically exhibit sufficient charge storage capacity, resulting in higher specific capacitance across all samples. Notably, the sample activated at 500 °C demonstrates the highest specific capacitance at low current density, indicating a robust charge storage ability at this temperature. Conversely, the sample activated at 400 °C, characterized by a simpler pore structure, high charge transfer resistance, and limited electrolyte ion penetration, shows lower specific capacitance. As current density increases, the specific capacitance decreases gradually for all samples, with a significant decline observed in the sample activated at 400 °C. This decrease may be attributed to its irregular pore structure or larger pore size, restricting ion transport efficiency. At activation temperatures of 500 °C and 600 °C, the samples continue to demonstrate favorable specific capacitance, indicating sustained pore structure and conductivity performance at moderate current densities.

Electrochemical impedance spectroscopy (EIS) was conducted across a frequency range of 10 mHz to 100 kHz with an open circuit potential of 5 mV to evaluate the electrochemical behavior of the six electrode materials, as depicted in Fig. 6c and detailed in Table 2. The equivalent circuit diagram used for EIS fitting is illustrated in Fig. S5. The point

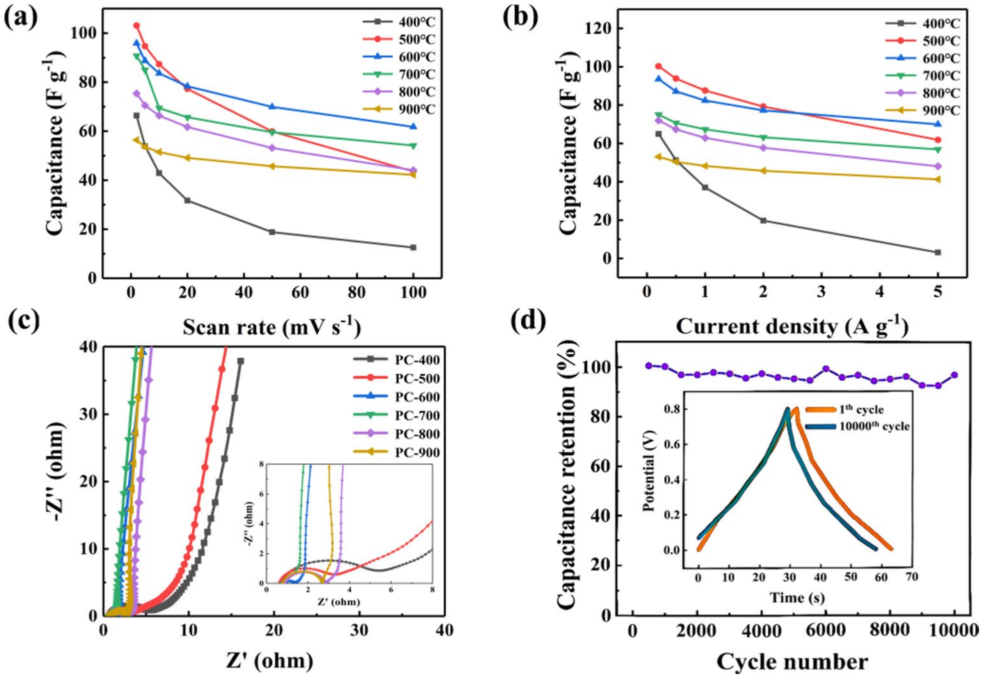

Fig. 6 **(a)** Specific capacitance for PC-*x* based supercapacitor at varied scan rates from CV curves; **(b)** Specific capacitance for PC-*x* based supercapacitor at varied current densities from GCD curves; **(c)** Nyquist plots of PC-x based supercapacitor in a frequency from 0.01 to 100 kHz. Insets display enlarged EIS plots in the high-frequency range.; **(d)** Cycling durability of the PC-500 electrode at a current density of 2 A g^{-1}, with the inset displaying the GCD curves for both the first and final cycles

of intersection of the EIS curves with the real axis signifies the intrinsic resistance (R_s) of the electrodes, encompassing the resistance of the current collector, intrinsic electrode material resistance, and contact resistance between them. The semicircular domain observed in the high-frequency range corresponds to the charge transfer resistance (R_{ct}), predominantly influenced by the formation of the electrochemical double layer [51]. In the low-frequency range, the EIS curves of the PC-*x* supercapacitors deflect towards the imaginary axis, indicating the superior capacitive behavior of the okra stem-based supercapacitors [52]. The initial point where the curve intersects the real axis represents the equivalent series resistance (ESR) of the electrode materials [7]. In Fig. 6c, for PC-400 and PC-500, the relatively higher R_{ct} values (3.586 and 2.045 Ω, respectively) can be attributed to incomplete removal of residual non-carbon components at lower activation temperatures, which may generate less uniform pore structures and hinder charge transfer [53]. The long-term stability of the electrodes was evaluated through galvanostatic charge-discharge (GCD) measurements at a current density of 2 A g^{-1}. After 10,000 charge-discharge cycles, the PC-500-based supercapacitor retained 97% of its initial capacitance, underscoring the exceptional cycling stability of the okra stem-derived carbon materials (Fig. 6d). This remarkable stability is primarily attributed to the moderate activation temperature (500 °C), striking a balance between pore structure, chemical stability, and mechanical strength, thereby enabling the carbon materials to maintain a high capacitance retention rate over extended cycling period [54, 55].

Table 3 compares the obtained results with those of various biomass-derived activated carbons from the last three years. The capacitance values either match or exceed those of most other carbon materials in aqueous electrolytes. Additionally, Fig. S6 illustrates the Ragone chart for the symmetric supercapacitor derived from okra stems in H_2SO_4 electrolyte, demonstrating an energy density of 8.9 Wh kg^{-1} and a power density of 80 W kg^{-1}, with the power density peaking at 2000 W kg^{-1}. These values either surpass or are in line with those documented for biomass-derived supercapacitors in prior research (See Table S1).

Utilizing okra waste at a lower activation temperature, microporous carbon materials are synthesized, with PC-500 displaying exceptional electrochemical performance attributed to its microporous configuration. The significance of this structure lies in its ability to facilitate the formation of the electrochemical double layer, particularly at lower current densities. This microporous architecture is a result of the inherent vascular bundle structure in okra stems, streamlining the activation process and reducing the required temperature. Lower activation temperatures equate to decreased energy consumption, facilitating the large-scale production of biomass-derived carbon materials for integration into energy storage systems.

4 Conclusion

This study pioneers the utilization of okra stem-derived carbon materials to fabricate activated carbon electrodes with enhanced porous structures via carbonization and KOH activation processes. By optimizing the activation temperature, both the pore architecture and conductivity of the electrodes exhibit significant enhancements. Particularly, electrodes treated at 500 °C maintain a microporous structure while ensuring excellent conductivity, resulting in outstanding performance in supercapacitor applications. The symmetrical supercapacitor achieved a specific

Table 3 Capacitance comparison for various biomass-derived carbon materials

Biomass	Activation agent	Activation temperature (°C)	Electrolyte/ Electrode configuration	Current density (A g^{-1})	Specific capacitance (F g^{-1})	Ref.
corn stalk-derived	KOH	800	6 M KOH/3 E	0.1	103	[56]
Terminalia elliptica	H_3PO_4	400	6 M KOH/3 E	1	183.4	[57]
Eucalyptus leaves (N-doped)	$ZnCl_2$	700	2 M KOH/3 E	0.25	258	[58]
Hibiscus flower	KOH	800	6 M KOH/3 E	1	216	[20]
Dandelion flower stem	K_2FeO_4	700	6 M KOH/3 E	0.5	309	[59]
Dandelion flower stem	K_2FeO_4	700	1 M Li_2SO_4/2E	0.25	40	[59]
Puffed rice	KOH	800	6 M KOH/2 E	0.5	21.1	[26]
Lacquer wood	H_3PO_4	600	1 M H_2SO_4/3 E	0.2	354	[60]
Residual carbon	KOH-K_2CO_3	400	6 M KOH/2 E	0.5	52.5	[61]
Nigella sativa	KOH	900	6 M KOH/3 E	0.5	210	[62]
Waste coffee	KOH	800	6 M KOH/3 E	0.5	164.4	[63]
Waste coffee	KOH	800	6 M KOH/2 E	0.5	58.7	[63]
Okra stem	KOH	500	1 M H_2SO_4/2 E	0.2	100.3	This work

capacitance of 100.3 F g^{-1} at 0.2 A g^{-1}, and maintained 97% of its initial capacitance even after 10,000 GCD cycles, indicating significant cycling stability. This study introduces an efficient technique for transforming okra stem residues into high-performance carbon materials suitable for energy storage devices, showcasing their promise in renewable energy storage, electric devices, and diverse applications. The cost-effective and sustainable microporous carbon derived from okra stems holds significant potential for industrial utilization in high-performance energy storage technologies.

Supplementary Information The online version contains supplementary material available at https://doi.org/10.1007/s13399-025-06977-9.

Acknowledgements This work was financially supported by the National Key R & D Program of China (No. 2022YFC3006303).

Authors' contributions Wen Li: Methodology, Investigation, Data curation, Writing–original draft preparation. Mingyu Wu: Methodology, Investigation, Data curation, Writing–original draft preparation. Zejian Chen: Investigation, Data curation, Writing preparation. Jianxiong Zhao: Writing-review & editingRongke Sun: Investigation, Data curation. Xiao Zhang: Investigation, Data curation. Dongliang Ma: Validation.Yanqing Ma: Validation, Data curation, Writing-review & editing, Supervision. Lei Ma: Conceptualization, Supervision, Methodology, Validation, Writing- review & editing.

Data availability Data will be made available on request.

Declarations

Competing interests The authors declare that they have no known competing financial interests or personal relationships that could have appeared to influence the work reported in this paper.

References

1. Ruman UE, Khan A, Fahad HM, Asif M, Shaheen F, Aziz MH, Ahmad R, Alam M, Sharif S, Afzal S (2024) Biogenic-eco-friendly synthesized SnO2/CuO/FeO/PVP/RGO nanocomposite for enhancing energy density performance of hybrid supercapacitors. J Energy Storage 89:111643–111654. https://doi.org/10.1016/j.est.2024.111643
2. Wang J, Zhang X, Li Z, Ma Y, Ma L (2020) Recent progress of biomass-derived carbon materials for supercapacitors. J Power Sources 451:227794. https://doi.org/10.1016/j.jpowsour.2020.227794
3. Anil Kumar Y, Koyyada G, Ramachandran T, Kim JH, Sajid S, Moniruzzaman M, Alzahmi S, Obaidat IM (2023) Carbon materials as a conductive skeleton for supercapacitor electrode applications: a review. Nanomaterials (Basel) 13:1049–1084. https://doi.org/10.3390/nano13061049
4. Zhang Y, Pan H, Zhou Q, Liu K, Ma W, Fan S (2023) Biomass-derived carbon for supercapacitors electrodes – a review of recent advances. Inorg Chem Commun 153:110768–110785. https://doi.org/10.1016/j.inoche.2023.110768
5. Yao Y, Zhou W, Cai K, Wen J, Zhang X (2024) Advances in the study of the biological activity of polysaccharide-based carbon dots: a review. Int J Biol Macromol 281:135774–135787. https://doi.org/10.1016/j.ijbiomac.2024.135774
6. Chen D, Chen H, Kuang Z (2024) Cotton fiber-derived carbon decorated with MoS2 for high electromagnetic wave absorption. Mater Chem Phys 326:129844–129853. https://doi.org/10.1016/j.matchemphys.2024.129844
7. Sun R, Zhang X, Chen Z, Ma Y, Ma L (2023) Application of long fibrous coconut silk-based porous carbon in flexible supercapacitor. J Energy Storage 66:107410. https://doi.org/10.1016/j.est.2023.107410
8. Tee JX, Selvarajoo A, Arumugasamy SK (2022) Prediction of carbon sequestration of biochar produced from biomass pyrolysis by artificial neural network. J Environ Chem Eng 10:107640–107658. https://doi.org/10.1016/j.jece.2022.107640
9. Zhao X, Li C, Sha L, Yang K, Gao M, Chen H, Jiang J (2022) In-built fabrication of MOF assimilated porous hollow carbon from pre-hydrolysate for supercapacitor. Polymers 14:3377–3391. https://doi.org/10.3390/polym14163377
10. Yang Y, Zhang F, Wei K, Zhai B, Wang X (2022) Porous carbon microspheres with controlled porosity and graphitization degree for high-performance supercapacitor. J Electroanal Chem 918:116449–11659. https://doi.org/10.1016/j.jelechem.2022.116449
11. Zhang X, Li Z, Tian X, Ma Y, Ma L (2021) Highly ordered micropores activated carbon from long fiber biomass for high energy density supercapacitors. ChemistrySelect 6:13015–13023. https://doi.org/10.1002/slct.202103712
12. Zhang D, Sun L, Liu Q, Sun H, Wang Q, Li W, Li Z, Wang B (2021) Ultra-high specific surface area porous carbon derived from chestnut for high-performance supercapacitor. Biomass Bioenergy 153:106227–106236. https://doi.org/10.1016/j.biombioe.2021.106227
13. Tian X, Ma H, Li Z, Yan S, Ma L, Yu F, Wang G, Guo X, Ma Y, Wong C (2017) Flute type micropores activated carbon from cotton stalk for high performance supercapacitors. J Power Sources 359:88–96. https://doi.org/10.1016/j.jpowsour.2017.05.054
14. Qin L, Cao Y, Cui Z, Feng F (2025) Rapid fabrication of mesoporous N- and P-codoped carbon from corn straw for advanced supercapacitor applications. J Energy Storage. https://doi.org/10.1016/j.est.2024.114849
15. Guo L, Jiao S, Wei G, Zhao X, Zhang J, Zhang H, Zhao X, Chen H, Ji X (2025) Regulating the pore structure and heteroatom doping of soybean straw carbon based on a bifunctional template method for the high-performance carbon supercapacitor. ChemSusChem 18:e202400780. https://doi.org/10.1002/cssc.202400780
16. Duman MN, Kocak ED, Merdan N, Mistik I (2017) Nonwoven production from agricultural okra wastes and investigation of their thermal conductivities. IOP Conference Series: Materials Science and Engineering 254:192007. https://doi.org/10.1088/1757-899X/254/19/192007
17. Teng Z, Han K, Cao Y, Qi J, Wang M, Liu J, Li Y (2025) N-doped porous carbon derived from different lignocellulosic biomass models for high-performance supercapacitors: the role of lignin, cellulose and hemicellulose. Int J Biol Macromol. https://doi.org/10.1016/j.ijbiomac.2024.138815
18. Majhi E, Deshpande AS, Batteries (2025) & Supercaps n/a:2500160. https://doi.org/10.1002/batt.202500160
19. Sun C, Tan H, Zhang Y (2023) Simulating the pyrolysis interactions among hemicellulose, cellulose and lignin in wood waste under real conditions to find the proper way to prepare bio-oil. Renew Energy 205:851–863. https://doi.org/10.1016/j.renene.2023.02.015
20. Zhu L, Wang Q, Wang H, Zhao F, Li D (2022) One-step chemical activation facilitates synthesis of activated carbons from *Acer truncatum* seed shells for premium capacitor electrodes. Ind

Crops Prod 187:115458–115470. https://doi.org/10.1016/j.indcrop.2022.115458

21. Hepsiba P, Rajkumar S, Elanthamilan E, Wang S-F, Princy Merlin J (2022) Biomass-derived porous activated carbon from *anacardium occidentale* shell as electrode material for supercapacitors. New J Chem 46:8863–8873. https://doi.org/10.1039/d2nj01041k
22. Kim D, Hadigheh SA, Wei Y (2024) Unlocking biosolid pyrolysis: towards tailored biochar with different surface properties. Mater Today Sustain 27:100868–110079. https://doi.org/10.1016/j.mtsust.2024.100868
23. Elanthamilan E, Jennifer SJ, Wang S-F, Merlin JP (2022) Effective conversion of *Cassia fistula* dry fruits biomass into porous activated carbon for supercapacitors. Mater Chem Phys 286:126188–126198. https://doi.org/10.1016/j.matchemphys.2022.126188
24. Aruchamy K, Dharmalingam K, Lee CW, Mondal D, Sanna Kotrappanavar N (2022) Creating ultrahigh surface area functional carbon from biomass for high performance supercapacitor and facile removal of emerging pollutants. Chem Eng J 427:131477–131489. https://doi.org/10.1016/j.cej.2021.131477
25. Deng L, Zhao Y, Sun S, Feng D, Zhang W (2024) Preparation of corn straw-based carbon by carbonization-KOH activation two-step method: Gas–solid product characteristics, activation mechanism and hydrogen storage potential. Fuel 358:130134–130147. https://doi.org/10.1016/j.fuel.2023.130134
26. Xie X, Zhang B, Wang Q, Zhao X, Wu D, Wu H, Sun X, Hou C, Yang X, Yu R, Zhang S, Murugadoss V, Du W (2021) Efficient microwave absorber and supercapacitors derived from puffed-rice-based biomass carbon: effects of activating temperature. J Colloid Interface Sci 594:290–303. https://doi.org/10.1016/j.jcis.2021.03.025
27. Qi F, Xia Z, Sun R, Sun X, Xu X, Wei W, Wang S, Sun G (2018) Graphitization induced by KOH etching for the fabrication of hierarchical porous graphitic carbon sheets for high performance supercapacitors. J Mater Chem A 6:14170–14177. https://doi.org/10.1039/c8ta01186a
28. Fu Y, Shen Y, Zhang Z, Ge X, Chen M (2019) Activated bio-chars derived from rice husk via one- and two-step KOH-catalyzed pyrolysis for phenol adsorption. Sci Total Environ 646:1567–1577. https://doi.org/10.1016/j.scitotenv.2018.07.423
29. Zhao R, Hao J, Yang X, Zhao Y, Chen J, Guo J, Chi C, Guo Q (2024) FeCl3 induced catalytic activation prepared porous carbon with carbon nanotube skeleton from coal for supercapacitor electrodes. J Power Sources. https://doi.org/10.1016/j.jpowsour.2024.235436
30. Zhang R, Wang Z, Zhao R, Lin Z, Yoo CG, Yang G, Chen J, Lyu G (2024) Construction of cellulose 3D network composite membrane supported by hydroxylated boron nitride with high surface charge density to achieve high-efficiency osmotic energy harvesting. Chem Eng J 500:157000–157012. https://doi.org/10.1016/j.cej.2024.157000
31. Vinu M, Prabu S, Virgin A, Chiang K-Y, Srivastava B, Ranjithkumar R (2025) Pre-carbonization of B/N/O heteroatom-codoped hierarchical porous carbon spheres derived from bio-waste orange peel for high-performance supercapacitors. Mater Res Bull 189:113441. https://doi.org/10.1016/j.materresbull.2025.113441
32. Sheng Z, Tang Z, Sun Y, Chen E, Hou D, Han X, Li H, Wang Z, Xie X, Li X, Lin X (2025) Oxygen-doped porous carbon materials derived from multiple ginkgo-based biomass for enhanced zinc ion hybrid capacitors. Colloids Surf A Physicochem Eng Asp 726:137773. https://doi.org/10.1016/j.colsurfa.2025.137773
33. Zhang H, Shen Z, Zeng R, Liang Q, Liu H (2024) Insights into pyrolysis product characteristics and carbon structure evolution of bituminous coal under high-temperature thermal shock. Fuel 371:132096–132107. https://doi.org/10.1016/j.fuel.2024.132096
34. Jaidan Jauhari, Almafie MR, Marlina L, Nawawi Z, Sriyanti I (2021) Physicochemical properties and performance of graphene oxide/polyacrylonitrile composite fibers as supercapacitor electrode materials. RSC Adv 11:11233–11243. https://doi.org/10.1039/D0RA10257A
35. Kong L, Li C, Sun R, Zhang S, Wang Y, Xiang J, Hu S, Wang D, Leng C, Hu X (2024) Thermal pretreatment of Willow branches impacts yield and pore development of activated carbon in subsequent activation with ZnCl2 via modifying cellulose structure. Chin J Chem Eng 69:227–237. https://doi.org/10.1016/j.cjche.2024.01.014
36. Reshma RP, Abishek NS, Gopalakrishna KN (2024) Synthesis and characterization of graphene oxide, tin oxide, and reduced graphene oxide-tin oxide nanocomposites. Inorg Chem Commun 165:112451–112463. https://doi.org/10.1016/j.inoche.2024.112451
37. Mehdi R, Naqvi SR, Khoja AH, Hussain R (2023) Biomass derived activated carbon by chemical surface modification as a source of clean energy for supercapacitor application. Fuel 10.1016/j.fuel.2023.128529:128529-12839. https://doi.org/10.1016/j.fuel.2023.128529
38. Gongxiang S, Yankui W, Dexin H, Hanjian L, Abdullahi SA, Jun X, Long J, Yi W, Sheng S, Song H, Jun X (2022) The heating rate and final temperature impacts on the coconut shell char structure characteristics during photo-thermal pyrolysis. J Anal Appl Pyrolysis 167:105695–105702. https://doi.org/10.1016/j.jaap.2022.105695
39. Dhashnamoorthy N, Nandhakumar B, Kumar RK, Radhamani AV (2025) Biomass to carbon nanoarchitectonics: ultrahigh-surface area micro-mesoporous activated carbon synthesized from palmyra palm tree flowers for advanced eco-friendly supercapacitors. Diamond Relat Mater 159:112785. https://doi.org/10.1016/j.diamond.2025.112785
40. Guye ME, Dabaro MD, Kim H (2025) Biomass-derived graphitic-like hierarchical porous carbon for electrochemical supercapacitor application. J Energy Storage 115:116037. https://doi.org/10.1016/j.est.2025.116037
41. Chen Y, Liu X, Ma X, Xia J, Yan D, Diao R, Zha Z, Qi F, Ma P (2025) Biomass-based 2D porous carbon with cross-linked nanosheets via co-hydrothermal pretreatment for high-performance supercapacitors. Chem Eng J 519:165145. https://doi.org/10.1016/j.cej.2025.165145
42. Cheng Z, Wu H, Zhang H, Wang Z, Wang L, Zou X, Zhu G (2024) Synthesis of cuprous organic frameworks with adjustable pores as membrane materials for C3H6/C3H8 separation. Small Struct 2:95–105. https://doi.org/10.1002/sstr.202400295
43. Tian X, Zhu S, Peng J, Zuo Y, Wang G, Guo X, Zhao N, Ma Y, Ma L (2017) Synthesis of micro- and meso-porous carbon derived from cellulose as an electrode material for supercapacitors. Electrochim Acta 241:170–178. https://doi.org/10.1016/j.electacta.2017.04.038
44. Kumar TR, Senthil RA, Pan Z, Pan J, Sun Y (2020) A tubular-like porous carbon derived from waste American poplar fruit as advanced electrode material for high-performance supercapacitor. J Energy Storage 32:101903. https://doi.org/10.1016/j.est.2020.101903
45. Zhang B, Xu Y, Wang J, Ma X, Hou W, Xue X (2021) Electrochemical performance of LiFePO4/graphene composites at low temperature affected by preparation technology. Electrochim Acta 368:137575–137582. https://doi.org/10.1016/j.electacta.2020.137575
46. Huo S, Zhao Y, Zong M, Liang B, Zhang X, Khan IU, Li K (2020) Enhanced supercapacitor and capacitive deionization boosted by constructing inherent N and P external defects in porous carbon framework with a hierarchical porosity. Electrochim Acta 353:136523–136534. https://doi.org/10.1016/j.electacta.2020.136523

47. Schalenbach M, Durmus YE, Tempel H, Kungl H, Eichel R-A (2021) Double layer capacitances analysed with impedance spectroscopy and cyclic voltammetry: validity and limits of the constant phase element parameterization. Phys Chem Chem Phys 23:21097–21105. https://doi.org/10.1039/d1cp03381f
48. Zhang Y, Li X, Li Z, Yang F (2024) Evaluation of electrochemical performance of supercapacitors from equivalent circuits through cyclic voltammetry and galvanostatic charge/discharge. J Energy Storage 86:111122–111130. https://doi.org/10.1016/j.est.2024.111122
49. Tsai WT, Ayestas R, Tsai CH, Lin YQ (2022) Preparation and characterization of porous materials from pineapple peel at elevated pyrolysis temperatures. Mater Basel 15:4686–4698. https://doi.org/10.3390/ma15134686
50. Zhao Z, Wang Z, Yu Y, Hu Y (2023) Localized electron density regulation effect for promoting solid-liquid ion adsorption to enhance areal capacitance of micro-supercapacitors. Small 19:2302489–2302500. https://doi.org/10.1002/smll.202302489
51. Liang K, Chen Y, Wang S, Wang D, Wang W, Jia S, Mitsuzakic N, Chen Z (2023) Peanut shell waste derived porous carbon for high-performance supercapacitors. J Energy Storage 70:107947–107958. https://doi.org/10.1016/j.est.2023.107947
52. Morad M, Mohamed S, AbouShahba R, Rashad M (2022) Preparation of perovskite-type ZnSnO3 nanoparticles and enhancing their behavior as a positive electrode for supercapacitor applications. Bull Tabbin Inst Metall Stud (TIMS) 111:19–30. https://doi.org/10.21608/tims.2022.158162.1004
53. Shandilya M, Kaur GA, Rai R (2021) Low temperature consequence on structural and impedance properties of BST ceramics via sol-hydrothermal method. Mater Chem Phys 263:124422–124434. https://doi.org/10.1016/j.matchemphys.2021.124422
54. Chatterjee D, Naik KG, Vishnugopi BS, Mukherjee PP (2024) Electrodeposition stability landscape for solid-solid interfaces. Adv Sci Weinh 11:2307455–2307466. https://doi.org/10.1002/advs.202307455
55. Li S, Xing T, Wang Y, Lu P, Kong W, Li S, Su X, Wei X (2021) Pore structure regulation and electrochemical performance characterization of activated carbon for supercapacitors. Front Energy Res 9:680761–680773. https://doi.org/10.3389/fenrg.2021.680761
56. Zhang Y, Cai Y, Li T, Wang M, Chen X, Xu Y (2024) Synthesis and electrochemical performance of biomass-derived porous carbon materials for supercapacitors. J Mater Sci Mater Electron 35:116–128. https://doi.org/10.1007/s10854-024-11944-7
57. Shrestha D (2024) Structural and electrochemical evaluation of renewable carbons and their composites on different carbonization temperatures for supercapacitor applications. Heliyon 10:e25628. https://doi.org/10.1016/j.heliyon.2024.e25628
58. Bejjanki D, Banothu P, Kumar VB, Kumar PS (2023) Biomass-derived N-doped activated carbon from Eucalyptus Leaves as an efficient supercapacitor electrode material. C. https://doi.org/10.3390/c9010024
59. Tan Y, Xu Z, He L, Li H (2022) Three-dimensional high graphitic porous biomass carbon from dandelion flower activated by K2FeO4 for supercapacitor electrode. J Energy Storage 52:104889–104898. https://doi.org/10.1016/j.est.2022.104889
60. Hu S-C, Cheng J, Wang W-P, Sun G-T, Hu L-L, Zhu M-Q, Huang X-H (2021) Structural changes and electrochemical properties of lacquer wood activated carbon prepared by phosphoric acid-chemical activation for supercapacitor applications. Renew Energy 177:82–94. https://doi.org/10.1016/j.renene.2021.05.113
61. Liu R, Wen J, Song J, Xin G, Bao J, Gao J, Wang Y (2025) One-step and low-temperature KOH-K2CO3 synergistic activation of residual carbon from coal gasification slag for supercapacitor electrode material. Ionics 31:3607–3618. https://doi.org/10.1007/s11581-024-06044-9
62. Teymur YA, Güzel F, İnal İIG (2023) High surface area mesoporous carbon from black cumin (*Nigella sativa*) processing industry solid residues via single-stage K2CO3 assisted carbonization method: production optimization, characterization and its some water pollutants removal and supercapacitor performance. Diamond Relat Mater 135:109815–109829. https://doi.org/10.1016/j.diamond.2023.109815
63. Zeng F, Tan Z, Yang X, Wang X, Xu B (2024) N–self–doped hierarchically porous carbon materials from waste coffee grounds for symmetric supercapacitor. J Mater Sci Mater Electron 35:885–899. https://doi.org/10.1007/s10854-024-12643-z